

Atomic threshold-switching enabled MoS₂ transistors towards ultralow-power electronics

Qilin Hua ^{1,2,3,6}, Guoyun Gao^{2,3,6}, Chunsheng Jiang^{1,6}, Jinran Yu^{2,3}, Junlu Sun², Taiping Zhang⁴, Bin Gao ¹✉, Weijun Cheng¹, Renrong Liang¹, He Qian¹, Weiguo Hu^{2,3}, Qijun Sun ^{2,3}✉, Zhong Lin Wang ^{2,3,5}✉ & Huaqiang Wu ¹✉

Power dissipation is a fundamental issue for future chip-based electronics. As promising channel materials, two-dimensional semiconductors show excellent capabilities of scaling dimensions and reducing off-state currents. However, field-effect transistors based on two-dimensional materials are still confronted with the fundamental thermionic limitation of the subthreshold swing of 60 mV decade⁻¹ at room temperature. Here, we present an atomic threshold-switching field-effect transistor constructed by integrating a metal filamentary threshold switch with a two-dimensional MoS₂ channel, and obtain abrupt steepness in the turn-on characteristics and 4.5 mV decade⁻¹ subthreshold swing (over five decades). This is achieved by using the negative differential resistance effect from the threshold switch to induce an internal voltage amplification across the MoS₂ channel. Notably, in such devices, the simultaneous achievement of efficient electrostatics, very small sub-thermionic subthreshold swings, and ultralow leakage currents, would be highly desirable for next-generation energy-efficient integrated circuits and ultralow-power applications.

¹Institute of Microelectronics, Beijing Innovation Center for Future Chips (ICFC), Tsinghua University, 100084 Beijing, China. ²CAS Center for Excellence in Nanoscience, Beijing Key Laboratory of Micro-nano Energy and Sensor, Beijing Institute of Nanoenergy and Nanosystems, Chinese Academy of Sciences, 101400 Beijing, China. ³School of Nanoscience and Technology, University of Chinese Academy of Sciences, 100049 Beijing, China. ⁴Department of Electrical Engineering, Tsinghua University, 100084 Beijing, China. ⁵School of Materials Science and Engineering, Georgia Institute of Technology, Atlanta, GA 30332-0245, USA. ⁶These authors contributed equally: Qilin Hua, Guoyun Gao, Chunsheng Jiang. ✉email: gaob1@tsinghua.edu.cn; sunqijun@binn.cas.cn; zhong.wang@mse.gatech.edu; wuhq@tsinghua.edu.cn

Scaling-down of complementary metal–oxide–semiconductor (CMOS) field-effect transistors (FETs) is a mainstream approach for reducing power dissipation in the rapidly developing field of information technology^{1–4}. However, CMOS technology still faces a great challenge of feature size <5 nm, due to the degradation of the off-state leakage current induced by short-channel effects (i.e., direct source–drain punch through, and a loss of gate electrostatic control)^{3–8}. An efficient way to minimize power consumption is to achieve a steep subthreshold swing (SS) with a fast-switching rate at a reduced supply voltage^{7,9}. The emerging two-dimensional (2D) transition metal dichalcogenides^{10–12}, e.g., atomically thin molybdenum disulfide (MoS₂)^{5,8,13}, are promising channel materials for future electronic chips with scaling dimensions and ultralow off-state currents, due to the high electron effective mass, low dielectric constant, and large bandgap^{10–13}. Furthermore, the atomic-scale thickness and smoothness of MoS₂ also significantly improve the electrostatic gate control capability according to its characteristic scaling length and can efficiently lower the supply voltage^{8,10}. However, the electrons in the source usually represent a thermal Boltzmann distribution with a potential barrier, which restricts the gate modulation capacity to 60 mV decade^{−1}, as determined by the thermal voltage (kT/q)^{6,7}. Hence, to break the “Boltzmann tyranny”, enabling atomic-scale FETs with steep subthreshold behavior and still maintaining high on/off current ratio, is critical for the development of ultralow-power electronics.

Several strategies have been proposed to obtain an SS of sub-60 mV decade^{−1}, such as band-to-band tunneling⁸, impact ionization¹⁴, nanoelectromechanical switching¹⁵, Dirac-source¹⁶, negative capacitance (NC)^{17–20}, and negative differential resistance (NDR)^{21,22}. The demonstrated threshold-switching behavior acting as an internal amplifier offers a shortcut to conquer the Boltzmann limit and triggers the FET to switch with a sub- kT/q slope. In particular, the NDR effect in threshold-switching FET is highly predictable and quantifiable for constructing steeply switchable electronic devices with high performance^{9,21}. When compared to a common insulator–metal–transition device (e.g., VO₂)^{21,23}, a new type of metal filamentary threshold switch (TS), which generally consists of Ag (or Cu) as an active electrode or dopant in a solid electrolyte, has been demonstrated a lower leakage current and much steeper switching characteristics^{24–27}, and can contribute to suppressing the off-state leakage current of conventional FETs with an abrupt SS^{22,28}. The seamless device architecture based on a 2D FET and TS may realize the simultaneous achievement of efficient electrostatic control, small sub-thermionic SS, and low leakage current, leading to efficiently minimizing power dissipation.

Here, we present an atomic threshold-switching MoS₂ FET (ATS-FET) with sharp on/off switching properties and ultralow energy consumption. The ATS-FET is endowed with an abrupt amplification capacity via integrating an abrupt variable-resistance Ag atomic TS with an atomically thin MoS₂ channel. The channel thickness and metal filament at the atomic scale are critical to reducing the supply voltage. The common HfO₂ insulator functions as the dielectric layer for the FET and the electrolyte for the TS, which is promising for future monolithic integration of the ATS-FET configurations with facile fabrication processes. The NDR effect according to the abrupt resistance transition of the TS induces an internal voltage amplification across the MoS₂ channel, which enables the MoS₂ FET to significantly overcome the fundamental thermionic limitation. According to the atomic thickness of the MoS₂ channel and the Ag atomic conductive filament (Ag filament), the superior electrical performances, such as on/off current ratio >10⁶, ultralow cutoff current at 1×10^{-13} A μm^{-1} , an average SS (SS_{average}) of sub-5 mV decade^{−1} (median), and very small hysteresis, are achieved in the ATS-FET. We systematically

investigate the influence of the NDR effect on the internal amplification phenomena and evaluate the improved electrical performance of the ATS-FET. The proposed ATS-FET has great potential to be extended to scalable and monolithic steep-slope transistor arrays and is of great significance in energy-efficient and high-performance electronic switches with ultralow-power dissipation.

Results

ATS-FET design. Figure 1a shows a schematic illustration of the ATS-FET by integrating an Ag atomic TS in series with a MoS₂ FET. The FET shares the same HfO₂ dielectric with the TS (acting as the electrolyte in the TS). Triangle-shaped MoS₂ nanoflakes are first synthesized on a SiO₂/Si substrate by chemical vapor deposition (CVD). The source/drain electrodes (Cr/Au) top-contacted with the MoS₂ are prepared via standard e-beam lithography (EBL), thermal evaporation, and lift-off process. The common HfO₂ thin film is deposited with atomic layer deposition (ALD), functioning as both the dielectric layer of the FET and the electrolyte of the TS. The Ag atomic layer is patterned on HfO₂ by a standard liftoff process. Top gate and drain contacts are defined at the desired position via EBL and metallization. The structural design of the common HfO₂ layer simplifies the fabrication process, while ensuring a high- κ dielectric performance for FET operation and good electrochemical kinetics for threshold switching. The fast formation and spontaneous rupture of the atomic Ag filament in the TS will lead to abrupt on/off switching in the ATS-FET with an ultralow SS (Fig. 1a).

Figure 1b depicts the equivalent circuit diagram of the ATS-FET, which can be considered as a baseline MoS₂ FET in series with a TS device. The supply voltage (or drain-to-source voltage, V_D) drives the TS and the MoS₂ channel, while the gate-to-source voltage (V_G) controls the switching characteristics of the ATS-FET. The supply voltage variably distributes between the TS and FET, corresponding to a voltage drop of V_D for the whole device and V_D' for the MoS₂ FET, respectively. Based on the series TS configuration, V_G can tune the Fermi level of the MoS₂ channel and lead to efficient control of the channel resistance, which dominantly determines the voltage drop between the FET and TS in the series configuration. The band diagrams of the ATS-FET for a typical V_G (compared with the threshold voltage, V_T) are illustrated in Fig. 1c, d. The HfO₂ electrolyte layer in the series TS can be considered as a variable barrier for electron transport according to the applied V_G , which determines the voltage drop on the MoS₂ channel and the TS component. For $V_G < V_T$, the Fermi level of MoS₂ is slightly shifted downward (the MoS₂ channel resistance is maintained at a high level). The current across the TS is insufficient to trigger the bridging of the Ag filament. The HfO₂ electrolyte layer acts as a large barrier to blocking the transport of electrons. When $V_G > V_T$, the MoS₂ Fermi level is effectively shifted downwards (the MoS₂ channel resistance transits to a low level). The current across the TS could induce the Ag filament formation, leading to an abrupt current increase (the mechanism will be discussed below in detail). An optical image of the ATS-FET device is shown in Fig. 1e. The TS stack (Au/Ag/HfO₂/Au) is connected in series to the FET, sharing its top electrode as the drain electrode of the ATS-FET. Figure 1f shows the Raman spectrum of a CVD synthesized MoS₂ nanoflake excited with a 532 nm laser. The peaks of the in-plane E_{2g} and out-of-plane A_{1g} vibration modes at 386.2 and 406.6 cm^{−1}, respectively, indicate that the as-grown MoS₂ is a monolayer.

ATS-FET versus the baseline FET. The transfer characteristics (I_D – V_G) of the ATS-FET and the baseline MoS₂ FET are presented

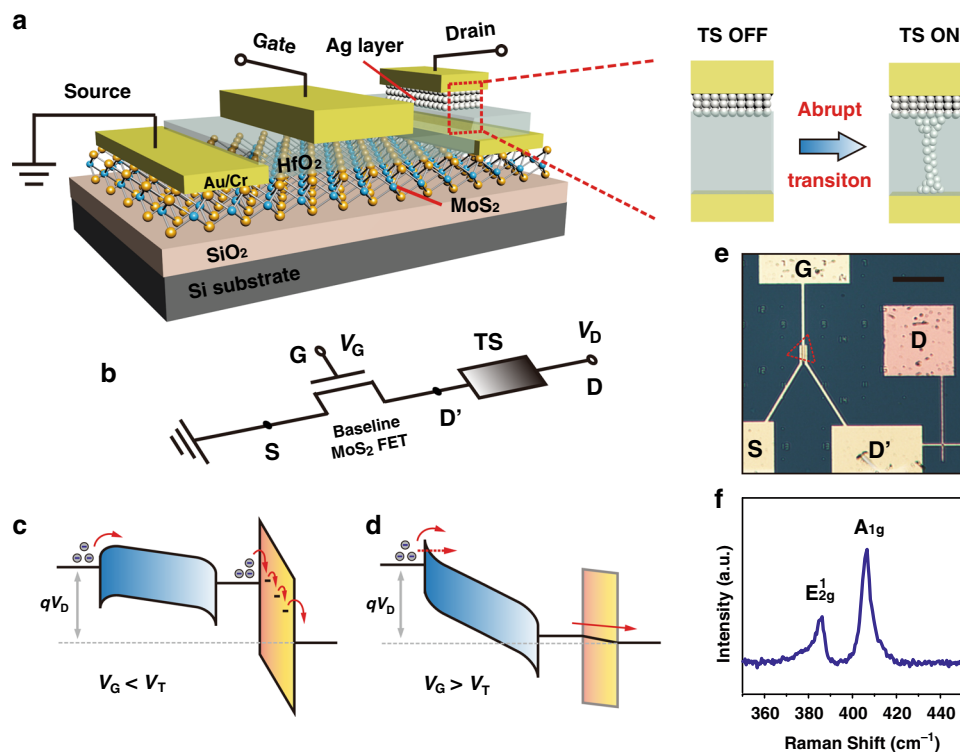


Fig. 1 Ultralow-power steep-slope 2D MoS₂ field-effect transistor with Ag atomic threshold-switching (ATS-FET). **a** Schematic illustration of the ATS-FET, consisting of a MoS₂ FET and an Ag/HfO₂ based TS. The enhanced performance of the ATS-FET is essentially attributed to the abrupt switching transition of the TS. **b** The equivalent circuit schematic of the ATS-FET, which can be considered as a baseline MoS₂ FET in series with a TS device. V_D is the drain-to-source voltage across the TS and the MoS₂ FET; V_G is the gate-to-source voltage across the MoS₂ FET. **c, d** Schematic band diagrams of the ATS-FET under thermal equilibrium with V_G bias, including **c** $V_G < V_T$ and **d** $V_G > V_T$. Electrons pass through the contact barriers via thermionic emission or tunneling; and across the electrolyte barrier via hopping. **e** Optical image of the ATS-FET device structure, exhibiting that the TS stack (cross-point area: $2 \times 2 \mu\text{m}^2$) in series with the channel of the MoS₂ FET. The red-dashed triangle indicates the MoS₂ channel material. Scale bar: $50 \mu\text{m}$. **f** Raman spectrum of the CVD synthesized MoS₂ nanoflake. The peaks of in-plane E_{2g} and out-of-plane A_{1g} vibrational modes are at 386.2 and 406.6 cm^{-1} , respectively.

in Fig. 2a. As is clearly shown, when V_G sweeps from -3 to 3 V and back to -3 V, the baseline MoS₂ FET exhibits an on/off current ratio of 10^5 and a very small hysteresis (grey square curves). The minimal SS (SS_{\min}) in forward and reverse sweeps are characterized to be 118.3 and $120.9 \text{ mV decade}^{-1}$, respectively, which are both above the thermionic limit of $60 \text{ mV decade}^{-1}$ at room temperature (Fig. 2b). In contrast, the ATS-FET shows more superior electrical properties, including a higher on/off current ratio (5×10^6), a lower off-state current ($1 \times 10^{-13} \text{ A } \mu\text{m}^{-1}$), and a much steeper SS ($< 5 \text{ mV decade}^{-1}$). It is remarkable that, in the ATS-FET, the series integration of a TS in the baseline MoS₂ FET enables to produce an internal amplification to overcome the fundamental thermionic limitation of the Boltzmann distribution of electrons. More impressively, the exponentially increased transfer curves of the baseline MoS₂ FET can transit to the nearly vertical transfer curves with much steeper slopes for the ATS-FET (Fig. 2a).

In the series combination, V_D is divided between the MoS₂ channel and the TS corresponding to their individual resistances. The off-state (or leakage) current of ATS-FET is commonly determined by the ultrahigh resistance of the TS, leading to a further decrease of I_D to a lower level of $1 \times 10^{-13} \text{ A } \mu\text{m}^{-1}$. Initially, at a low V_G , the I_D flowing through the MoS₂ channel and TS is insufficient to induce the switching of TS. As V_G increases (i.e., forward sweep), the MoS₂ channel resistance shows a gradual decrease until I_D approaches a critical threshold ($I_{\text{th-TS}}$), which is capable to induce the switching on of TS (to low-resistance state, LRS). And consequently, the total resistance of

the ATS-FET dramatically decreases and triggers an abrupt I_D increase. On the contrary, as V_G decreases (i.e., reverse sweep), the MoS₂ channel resistance shows a gradual increase until I_D reduces to another critical threshold ($I_{\text{hold-TS}}$), which could reversely induce the switching off of TS (back to high-resistance state, HRS) and causes a rapid drop of I_D . Hence, hysteresis in the transfer curve can be found as a result of the difference in V_G corresponding to the two critical thresholds (Fig. 2a). Different from that of the baseline FET (clockwise), the hysteresis of the ATS-FET resembles an anticlockwise transition that is caused by the series integration of the TS.

From the subthreshold region of the ATS-FET (in Fig. 2a), the extracted SS_{\min} in forward and reverse sweeps are 2.5 and $4.5 \text{ mV decade}^{-1}$, respectively, as shown in Fig. 2b. Besides, the ATS-FET has a large range of I_D (over four decades) where the average SS (SS_{average}) is $3.0 \text{ mV decade}^{-1}$ in the forward sweep. It is considered that the NDR effect originating from the volatile threshold-switching behavior in the atomic Ag filament device induces an efficient internal voltage amplification across the atomically thick MoS₂ channel, and contributes to inducing a record and significantly reduced SS, which is much smaller than the values previously reported for a tunnel FET (TFET) at $31.1 \text{ mV decade}^{-1}$ (ref. 8), an NC-FET at $41.7 \text{ mV decade}^{-1}$ (ref. 19), a Dirac-source CNT FET (DS-FET) at $35 \text{ mV decade}^{-1}$ (ref. 16), and an ion liquid gating FET at $50 \text{ mV decade}^{-1}$ (ref. 29). Moreover, the subthreshold characteristics of various types of the steep-slope MoS₂ FETs are outlined in Supplementary Table 1. A record on SS_{\min} of $0.3 \text{ mV decade}^{-1}$ and SS_{average} of 1.3 mV

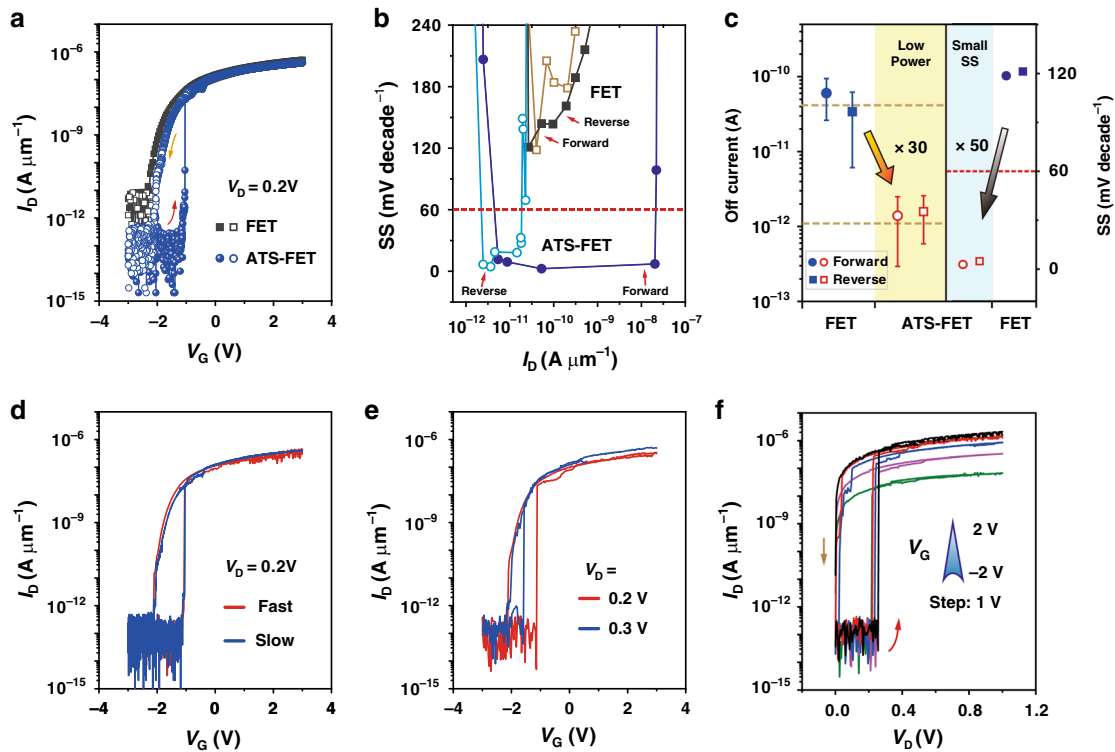


Fig. 2 Device performances of the ATS-FET. **a** Transfer curves from the ATS-FET and FET with the same 2D MoS₂ channel (channel width: 10 μm; channel length: 2 μm). Solid symbols indicate the forward sweep, while open symbols indicate the reverse sweep. **b** SS from the ATS-FET and FET both in forward and reverse sweeps. The FET operates well above the fundamental thermionic limitation, while the ATS-FET has a large range of the drain current where the minimal SS is 2.5 mV decade⁻¹. **c** The off-state leakage current and SS can be simultaneously reduced in the ATS-FET, indicating the ultralow-power steep-slope phenomenon in the ATS-FET. **d** I_D - V_G characteristics measured at room temperature and at $V_D = 0.2$ V at slow/fast gate voltage sweep speeds. The V_G steps were set to 3 and 30 mV, respectively. **e** Transfer characteristics (I_D - V_G) measured at room temperature and at $V_D = 0.2$ and 0.3 V. **f** Output characteristics (I_D - V_D) measured at room temperature at V_G from -2 to 2 V with a step of 1 V.

decade⁻¹ (over three decades) is also achieved in the ATS-FET at room temperature.

Both reductions in off-state current and SS in the ATS-FET. Power dissipation is a fundamental issue for advanced CMOS technology, which faces two severe challenges: the increasing difficulty for the supply voltage scaling, and the rising leakage currents causing on/off current ratio degradation^{6,7}. The energy efficiency of a logic operation can be estimated through the total switching energy (E_{total}) consisting of dynamic (E_{dynamic}) and static (E_{static}) parts, defined as:

$$\begin{aligned} E_{\text{total}} &= E_{\text{dynamic}} + E_{\text{static}} \\ &= \alpha C_L V_D^2 + I_{\text{off}} V_D \tau_{\text{delay}}, \\ &\approx C_L V_D^2 \left(\alpha + \gamma 10^{-\frac{V_D}{SS}} \right) \end{aligned} \quad (1)$$

where C_L is the switched capacitance, τ_{delay} is the delay time, α is the activity factor, and γ is a fitting parameter⁷. It can be inferred from the above equations that the steeper SS and a lower off-state current in FETs enable further scaling of the supply voltage and a corresponding reduction in total power dissipation. As shown in Fig. 2c (orange region), the integration of the TS with the baseline MoS₂ FET helps to significantly suppress the off-state leakage currents by ~30 times, attributing to the ultrahigh resistance of the TS in the off-state (~1 TΩ). Besides, SS_{min} of the ATS-FET in forward and reverse sweeps have been demonstrated to greatly decrease to 2.5 and 4.5 mV decade⁻¹, respectively. Both of them are far lower than the fundamental thermionic limitation and

those of the baseline MoS₂ FET (close to 50 times reduction, the cyan region of Fig. 2c).

Electrical properties of the ATS-FET. To exclude the effects of the V_G sweeping rate on the ultralow SS, the transfer characteristics (I_D - V_G) of the ATS-FET are measured at slow and fast V_G sweep speeds of 3 and 30 mV s⁻¹, respectively. As illustrated in Fig. 2d, identical steep-slope switching characteristics with high on/off current ratios over 10⁶ are observed at different V_G sweep speeds. The SS, V_T , off-state current, and on/off ratio are all independent of the V_G sweeping rate. In addition, the transfer characteristics (I_D - V_G) of the ATS-FET at $V_D = 0.2$ and 0.3 V are shown in Fig. 2e. In the forward sweep, the SS_{average} at $V_D = 0.2$ and 0.3 V are characterized to be 4.5 mV decade⁻¹ (over five decades) and 6.0 mV decade⁻¹ (over four decades), respectively. Meanwhile, V_T of the ATS-FET shows a negative shift from -1.14 to -1.59 V, which is determined by the balances between the supply voltage and the relevant potential drops on the FET and TS during the V_G sweeping. At a higher V_D , the TS favors a tendency for the turn on state; consequently, the abrupt resistance change is less efficient, and it is easier for the TS to be switched on at a lower V_G . In the reverse sweep, the I_D of the ATS-FET decreases until it reaches the critical threshold $I_{\text{hold-TS}}$ ($< 5 \times 10^{-11}$ A μm⁻¹), leading to the instantaneous switching off of the TS. And hence, the ATS-FET shows similar abrupt switching characteristics in the subthreshold region regardless of V_D . The output characteristics (I_D - V_D) of the ATS-FET for different V_G are characterized, as shown in Fig. 2f. The channel current I_D

increases from 6.7×10^{-8} to $2.1 \times 10^{-6} \text{ A } \mu\text{m}^{-1}$ as V_G increases from -2 to 2 V in the linear/saturation region, showing an increase in the channel conductance with increasing V_G . Distinguishable on- and off-states are observed in different V_D regions ($V_D < V_{\text{th-TS}}$ or $V_D \geq V_{\text{th-TS}}$, $V_{\text{th-TS}}$ is the threshold voltage of the TS), as shown in Fig. 2f. As V_D increases, when $V_D < V_{\text{th-TS}}$, the conductance of the ATS-FET is primarily determined by the TS, even though the MoS_2 channel is in a LRS; when $V_D \geq V_{\text{th-TS}}$, the conductance of the ATS-FET is coordinated by the MoS_2 channel. Similarly, as V_D decreases, the conductance of the ATS-FET shows a sudden reduction when $V_D \leq V_{\text{hold-TS}}$ ($V_{\text{hold-TS}}$ is the hold voltage of the TS). Moreover, the output characteristics of another ATS-FET and its baseline FET at different V_G (from -2 to 2 V) in linear scale are also demonstrated in Supplementary Fig. 1. It is clearly observed that the abrupt switching on/off behavior of TS contributes to causing the steep-slope phenomenon of the 2D FET.

Ag atomic threshold switching. The excellent subthreshold characteristics of the ATS-FET are attributed to the series integration of high-performance TS device. Therefore, it is critical to achieving a TS device with superior threshold-switching behavior. The typical I - V characteristic of the as-fabricated TS device at a compliance current (I_{cc}) of 100 nA is shown in Fig. 3a. The TS exhibits volatile threshold-switching behavior with a small threshold voltage of the TS ($V_{\text{th-TS}} = \sim 0.26 \text{ V}$), an ultralow leakage current ($< 1 \text{ pA}$), and a high on/off current ratio ($> 10^6$). The TS device switches from the off-state to the on-state at an applied voltage (V_a) larger than $V_{\text{th-TS}}$ (green curve in Fig. 3a), while it switches to the off-state at V_a less than the hold voltage ($V_{\text{hold-TS}}$; grey curve in Fig. 3a). The TS device yields an extremely steep on/off switching slope $< 0.5 \text{ mV decade}^{-1}$, and $V_{\text{th-TS}}$ ranges between 0.205 and 0.265 V in the cyclic tests. Energy-dispersive X-ray

spectroscopy (EDS) line profiles of the cross-sectional TS stack layers are shown in Fig. 3b. The inset is a high-angle annular dark-field scanning transmission electron microscopy (HAADF-STEM) image. The sphere-shaped Ag layer, HfO_2 dielectric layer, and top/bottom electrode (TE/BE) layers can be clearly observed, with the Ag atomic-scale layer accumulated at the interface of TE/ HfO_2 .

To investigate the effect of the filament morphology on the switching dynamics, the formation and rupture of the Ag filament at a V_a of 0.4 V are illustrated in Fig. 3c via a Monte Carlo simulation (the flow chart is shown in Supplementary Fig. 2). The on-/off-state of the TS is determined by the formation/rupture of Ag filament with volatile threshold-switching behavior. The HfO_2 electrolyte layer of the TS can be considered as a variable barrier for electron transport. The Ag nanoparticles diffusion into HfO_2 matrix contributes to electrons transport along the nanoparticle chain (i.e., filament), and the adjacent Ag nanoparticles can act as electron traps for thermionic emission or tunneling³⁰. As shown in Supplementary Fig. 3, the Arrhenius curve is used to explain the temperature dependence of the leakage current of a TS device. The charge transport of the TS at HRS is governed by a combination of Frenkel-Poole (F-P) emission and trap-assisted tunneling (TAT) process³¹⁻³³. Specifically, in the high-temperature region ($> 200 \text{ K}$), the current strongly depends on the temperature, indicating the F-P emission mechanism. In contrast, in the low-temperature region ($< 200 \text{ K}$), the current shows weak temperature-dependent behavior due to the existence of the TAT mechanism.

By applying a large voltage on the TS, the abrupt formation of the Ag filament commonly induces the NDR effect across the TS. The measured I - V characteristics of the TS device in voltage-sweeping and current-sweeping modes are shown in Supplementary Fig. 4, indicating good performances for current-controlled (or S-type) NDR behavior. The NDR effect is further illustrated with a control sample (the TS connected with a resistor R_L , Supplementary Fig. 5a) to study the distribution of the voltage drops during the on/off switching process of the TS. The NDR effect induces an abruptly decreased voltage drop ($V_{\text{TS}} - \Delta V_{\text{NDR}}$) across the TS device, and consequently an amplified voltage drop ($V_L + \Delta V_{\text{NDR}}$) across the series resistor (Supplementary Fig. 5a). The decrease in the voltage drop ($-\Delta V_{\text{NDR}}$) across the TS device can be extracted from the AC I - V characteristics (Supplementary Fig. 5b). According to the analysis of the control sample, it can be predicted that the NDR effect can induce a similar internal voltage amplification by replacing the resistor with a MoS_2 FET.

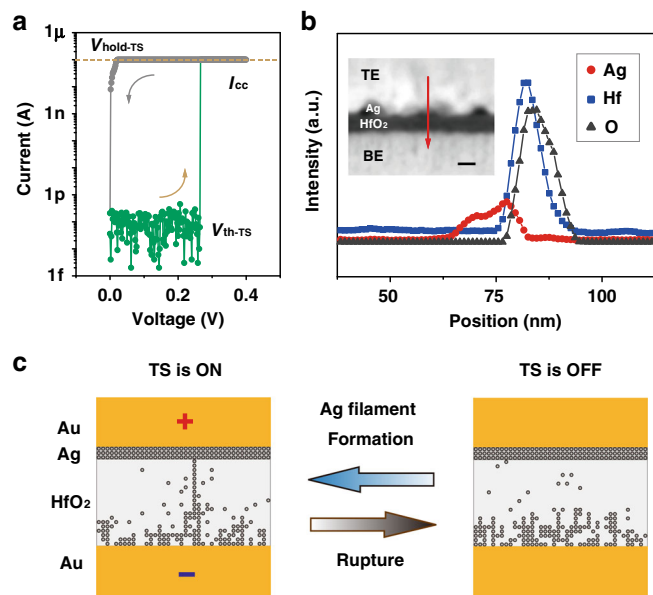


Fig. 3 Ag atomic threshold-switching (Ag/ HfO_2 -based TS). **a** Typical I - V characteristic of the TS device at a compliance current (I_{cc}) of 100 nA in forward (green)/reverse (grey) voltage sweeping, exhibiting ultralow leakage currents ($< 1 \text{ pA}$). **b** Energy-dispersive X-ray spectroscopy (EDS) line profiles (including Ag, Hf, and O elements) of the TS stack layers along the red line shown in a cross-sectional high-angle annular dark-field scanning transmission electron microscopy (HAADF-STEM) image. Scale bar: 10 nm . **c** Simulation for the formation and rupture procedures (on/off) of the atomic Ag filament in the TS device with an applied voltage of 0.4 V .

Monitoring the internal amplification in the ATS-FET. The equivalent circuit diagram of the ATS-FET can be considered as two variable resistors connected in series, as shown in Fig. 4a. We try to disclose the working mechanism of the ATS-FET by using mathematical derivation and simulation with a semi-quantitative model³⁴⁻³⁶, and the simulation is illustrated in Supplementary Fig. 6 and Note 1. Taking the highly nonlinear I - V characteristics both of TS and baseline MoS_2 FET into consideration, the node voltage (V_D) and the channel current (I_D) can be solved as the intersections of output characteristics (I_D - V_D , black lines) of the baseline MoS_2 FET and the I - V curve (I_D - V_D , red line) of TS device for different V_G (see Supplementary Fig. 6c). Impressively, the simulated transfer curves extracted from Supplementary Fig. 6c are in good agreement with the experimental data, as depicted in Fig. 4b. From a physical viewpoint, the steep SS phenomenon is caused by the NDR effect of TS, and it can be understood by a concept of internal amplification gain ($\beta = dV_D/dV_G$), which is defined to describe

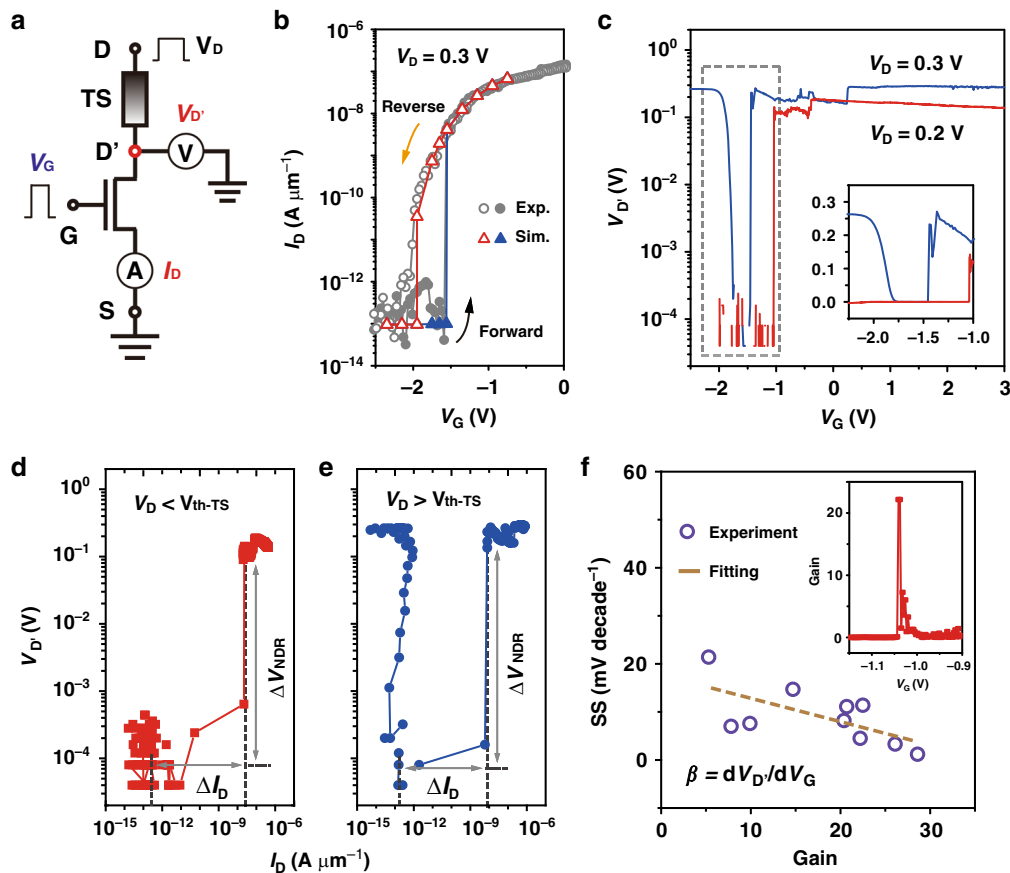


Fig. 4 ATs-FET with an internal amplification across the MoS₂ channel. **a** The equivalent circuit schematic for the electrical measurements. $V_{D'}$ and I_D in red are the output parameters that need to be simultaneously recorded with the increase of the input V_G (blue). **b** The experimental and simulated transfer (I_D - V_G) characteristics of the ATs-FET at $V_D = 0.3$ V, indicating the simulated results are in good agreement with the experimental data. **c** The relations between the gate voltage (V_G) and the internal voltage ($V_{D'}$) for two V_D schemes, including $V_D (= 0.2$ V) $< V_{th-TS}$ and $V_D (= 0.3$ V) $> V_{th-TS}$. The inset is the linear scale from the data shown in the dashed grey rectangle. **d, e** $V_{D'}$ changes as a function of I_D for the two V_D schemes. The NDR effect induces an amplification of $V_{D'}$ across the MoS₂ channel. **f** The relation between the average SS and the internal amplification gain ($\beta = dV_{D'}/dV_G$). The inset indicates the sharp increase in $V_{D'}$ with respect to the applied V_G occurring in the region of the abrupt switching due to the NDR effect.

the relationship between $V_{D'}$ and V_G . According to the definition of subthreshold swing, SS can be written as

$$\begin{aligned}
 SS &= \frac{\partial V_G}{\partial \log_{10}(I_D)} = \frac{\partial V_G}{\partial V_{D'}} \times \frac{\partial V_{D'}}{\partial \log_{10}(I_D)} = \frac{\frac{2.3kT}{q}}{\frac{1}{n} + \frac{\beta}{\exp(\frac{qV_{D'}}{kT}) - 1}} \\
 &\approx \frac{2.3kT}{q} \times \frac{\exp(\frac{qV_{D'}}{kT}) - 1}{\beta} \\
 &\approx 0 \text{ mV decade}^{-1}, \text{ when } \beta \rightarrow \infty,
 \end{aligned}
 \tag{2}$$

where $V_{D'}$ is the output voltage at the internal node D' , β is the internal amplification gain, n is the ideal factor, q is the basic electron charge, k is the Boltzmann constant, and T is the absolute temperature. Ideally, β is approximated to be infinity (i.e., $\Delta V_G = 0$) in the forward switching process, and thus SS will be approximated to be zero. However, due to the inevitable limitation by the accuracy of the testing instrument, the measured SS is >0 mV decade⁻¹.

To verify and further elaborate the internal amplification induced by the NDR, we monitor the output voltage at the internal node D' ($V_{D'}$) and analyze the voltammetry characteristics under current sweeping at two different V_D . According to V_{th-TS} at ~ 0.26 V, we reasonably select two typical V_D values (0.2 and 0.3 V, i.e., $V_D < V_{th-TS}$ and $V_D > V_{th-TS}$, respectively). As shown in Fig. 4c, the abrupt increases in $V_{D'}$ are clearly observed

under both V_D ($V_D < V_{th-TS}$ and $V_D > V_{th-TS}$). As V_G sweeps over V_{th-TS} , the redistribution of the effective potential drops on the MoS₂ channel and the TS pulls up (increases) $V_{D'}$ according to the drain voltage superposition effect. The $V_{D'}$ drop on the MoS₂ channel is amplified according to the NDR effect caused by the TS transition from the off-state to the on-state. Notably, the trends of the variation in $V_{D'}$ are obviously distinguishable for different V_D . $V_{D'}$ at $V_D = 0.3$ V shows an initial decrease with a subsequent increasing trend, while $V_{D'}$ at $V_D = 0.2$ V only shows an increase at the pull-up point. The pull-up V_G value also shifts from -1.45 to -1.04 V as V_D decreases from 0.3 to 0.2 V (inset of Fig. 4c). The underlying reason is explained by the voltammetry characteristics under current sweeping. For $V_D < V_{th-TS}$ (Fig. 4d), the TS is initially in the off-state at $I_D < 1 \times 10^{-12}$ A μm^{-1} . To maintain a low current in the series circuit, $V_{D'}$ is therefore kept at a low level to minimize the current in the MoS₂ FET. As I_D increases, $V_{D'}$ slightly increases. When I_D is large enough (exceeding 1.6×10^{-12} A μm^{-1}) to trigger the Ag filament formation in the TS, the resistance of the ATs-FET abruptly decreases with $V_{D'}$ representing a steep increment (ΔV_{NDR}). In contrast, $V_{D'}$ is initially at a high level (0.263 V) for $V_D > V_{th-TS}$ (Fig. 4e). This may be because the supply voltage applied from the drain electrode is transiently imposed on the TS component and triggers the bridging of the Ag filament. The instantly increased device current results in a high $V_{D'}$ at the beginning. Then, $V_{D'}$ dramatically decreases with a subsequent slight increasing

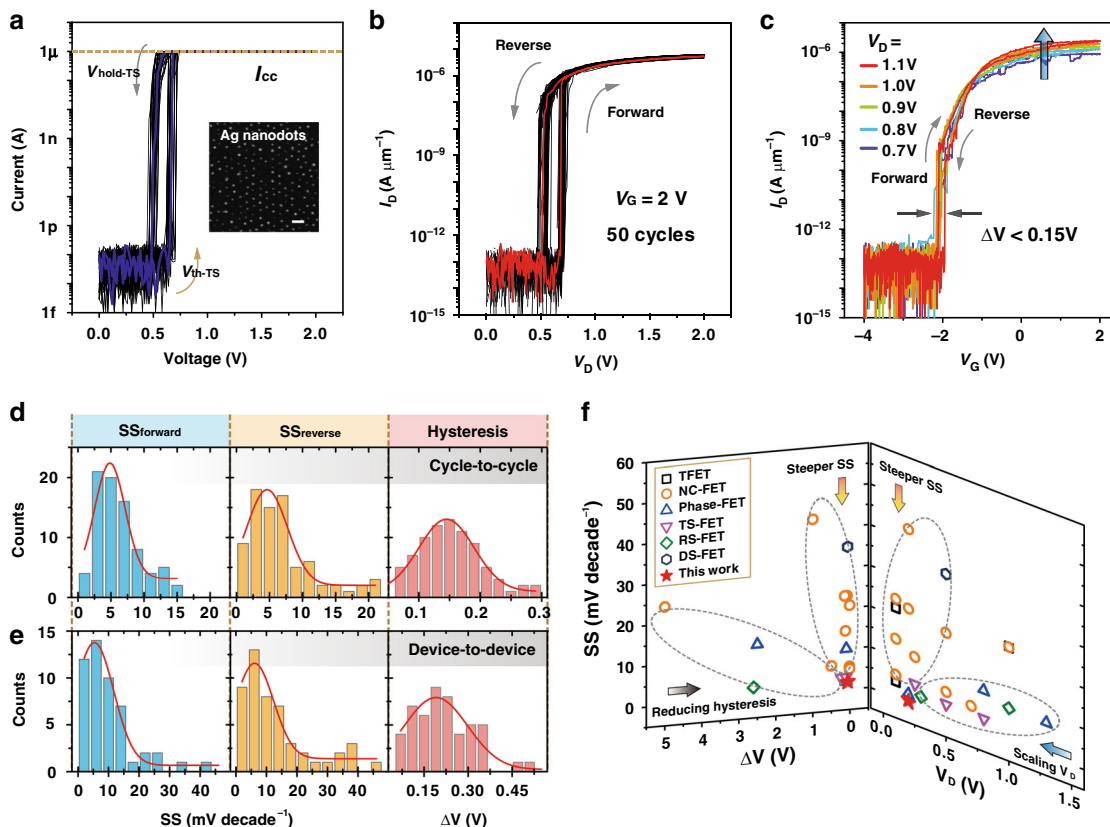


Fig. 5 ATs-FET with much-reduced hysteresis and SS. **a** Typical I - V characteristics of the TS device based on highly ordered Ag nanodots in 30 cycles ($I_{cc} = 1 \mu\text{A}$). The inset is a scanning electron microscopy (SEM) image of highly ordered Ag nanodots. **b** Output characteristics of the ATs-FET with the newly presented TS at $V_G = 2 \text{ V}$ in 50 cycles. 2D MoS_2 channel (channel width: $2.2 \mu\text{m}$; channel length: $1.8 \mu\text{m}$). **c** Transfer characteristics (I_D - V_G) of the ATs-FET with the newly presented TS at V_D ranging from 0.7 to 1.1 V. **d**, **e** Statistical distributions of SS_{forward} , SS_{reverse} and hysteresis (ΔV) of the ATs-FET in **d** cycle-to-cycle and **e** device-to-device variations. **f** Comparisons of SS- V_D (right) and SS- V_G (left) in different steep-slope FETs, including the TFET^{8,39,40}, NC-FET^{18-20,41-46}, phase-FET^{21,47,48}, Ag (or Cu) filament TS-FET^{22,28,49}, resistive-switching FET (RS-FET)^{50,51}, and DS-FET¹⁶, and our ATs-FET.

trend as I_D sweeps. When I_D exceeds $1.4 \times 10^{-12} \text{ A } \mu\text{m}^{-1}$, $V_{D'}$ represents a steep increment (ΔV_{NDR}). As the supply voltage in Fig. 4e is larger than that in Fig. 4d, the trigger current for the Ag filament would be relatively smaller, which is consistent with the results in Fig. 4c.

Furthermore, the internal amplification gain ($\beta = dV_{D'}/dV_G$) extracted from the abrupt switching region is ~ 22.2 for a low supply voltage at $V_D = 0.2 \text{ V}$ (the inset of Fig. 4f), corresponding to the SS_{min} of $2.5 \text{ mV decade}^{-1}$ and the SS_{average} of $3.0 \text{ mV decade}^{-1}$ over four decades of I_D . As the internal amplification gain increases to 28.6, the SS_{average} can be further reduced to a record of $1.3 \text{ mV decade}^{-1}$ (Fig. 4f). The internal amplification gain is considered a significant parameter for designing steeper-slope FETs with lower energy consumption.

Based on the above discussion, the internal voltage amplification in the ATs-FET according to the voltage snapback (ΔV_{NDR}) induced by the NDR effect is directly observed in this work. From the point of view of charge carriers, the free electrons transported in the ATs-FET are blocked by the barrier of the HfO_2 electrolyte at the beginning ($V_G < V_T$). When V_G reaches V_T , I_D increases in an abrupt fashion as a result of the Ag filament formation. Hence, the ATs-FET can in principle overcome the fundamental thermionic limitation of $60 \text{ mV decade}^{-1}$ at room temperature.

Improved ATs-FET with much-reduced hysteresis and SS. Hysteresis is commonly undesirable for transistors in logic applications³⁷. Technically, the achievable ATs-FET with small hysteresis (or hysteresis-free) and ultralow subthreshold

characteristics is capable to offer the promising potential for ultralow-power logic circuit applications. However, the ATs-FET described above exhibits large hysteresis of 0.5–1 V (Fig. 2), which in essence needs to be greatly reduced. Some device optimization methods were used to reduce the hysteresis, such as annealing, and passivation, as previously reported^{37,38}. To suppress the hysteresis of the ATs-FET, we also present an effective approach of device optimization by using the TS device with highly ordered Ag nanodots, which could contribute to shrinking the switching window (e.g., reducing the difference between $V_{\text{th-TS}}$ and $V_{\text{hold-TS}}$) and improving $I_{\text{hold-TS}}$ of TS. The newly presented TS device is fabricated with a HfO_2 layer of 10 nm, an active electrode of highly ordered Ag nanodots, and followed by a process of rapid thermal annealing. It is critical to treat the atomic Ag layer with rapid thermal annealing to make the Ag atoms accumulate in a spherical shape, which is preferential for interstitial dopants in HfO_2 to guarantee the volatile threshold-switching behavior even at a high-compliance current²⁶. With the compliance currents (I_{cc}) defined from 10 nA to $50 \mu\text{A}$, the TS device shows abrupt and volatile threshold-switching behavior (Supplementary Fig. 7a). And the TS device also exhibits good stability in the cyclic test (Fig. 5a), achieving a reduced switching window of 0.12–0.24 V and small variations both in $V_{\text{th-TS}}$ and $V_{\text{hold-TS}}$ (Supplementary Fig. 7b). Furthermore, by connecting such TS device to a MoS_2 FET, an improved ATs-FET is demonstrated to have much-reduced hysteresis and SS in a highly reproducible manner. The output characteristics (I_D - V_D) of the improved ATs-FET for different V_G are shown in Supplementary Fig. 8.

Fifty continuous cycles of the output characteristics (at $V_G = 2$ V) in Fig. 5b can also verify the stable and repeatable operations of the ATS-FET. From the transfer characteristics in Fig. 5c, we can see that the improved ATS-FET shows reduced hysteresis of <0.15 V at different V_D (ranging from 0.7 to 1.1 V). More impressively, the nearly negligible hysteresis (10 mV) is observed at the V_D of 0.7 V, meanwhile the SS_{\min} in forward and reverse sweeps are 2.6 and 12.5 mV decade $^{-1}$, respectively (Supplementary Fig. 9). Further extracting key parameters, including SS_{forward} , SS_{reverse} , hysteresis, and V_T , from three ATS-FETs are shown in Supplementary Fig. 10. The SS_{forward} , SS_{reverse} , and hysteresis are all independent of V_D , while the V_T shows the negative shift with the increase of V_D (consistent with that of Fig. 2e).

Statistical analysis of ATS-FET and the device comparison. To more clearly illustrate the reproducibility of the ATS-FET, we conduct the statistical analysis for the average SS (including SS_{forward} and SS_{reverse}), and hysteresis in cycle-to-cycle (80 cycles) and device-to-device (50 devices) variations. Figure 5d shows the histograms and Gaussian fits for the SS_{forward} , SS_{reverse} , and hysteresis (4.8 and 4.6 mV decade $^{-1}$; 0.14 V) of the ATS-FET in 80 cycles. Besides, the abrupt switching behavior of the ATS-FET is free of device-to-device deviations. The Gaussian distributions of the SS_{forward} , SS_{reverse} , and hysteresis are plotted in Fig. 5e, showing that the statistical SS_{forward} , SS_{reverse} , and hysteresis mainly distribute at 5.3 mV decade $^{-1}$, 6.1 mV decade $^{-1}$, and 0.19 V, respectively.

According to the above-described Eq. (1), V_D and SS synergistically contribute to the evaluation of power consumption in the FET device. And hence, it is recommended that both V_D and SS are preferred to be minimized, in addition to the suppressed hysteresis in transfer curves. Compared with previous reports of different categories of steep-slope transistors, including the TFET^{8,39,40}, NC-FET^{18–20,41–46}, phase-FET^{21,47,48}, Ag (or Cu) filament TS-FET^{22,28,49}, resistive-switching FET^{50,51}, and DS-FET¹⁶, the relations of SS–hysteresis and SS– V_D are both summarized and depicted in Fig. 5f. Capable of achieving steeper SS, reducing hysteresis, and scaling V_D , the ATS-FETs show superior performances by using the atomic-scale geometry design with seamless integration of 2D FET and TS. Specifically, the achieved ATS-FET is nearly hysteresis free (10 mV), and has ultralow SS_{\min} of <2.6 mV decade $^{-1}$, which can satisfy the ITRS requirement for the SS of 25 mV decade $^{-1}$ in the year of 2027 (ref. 1), and will be promising for future electronics with ultralow-power consuming.

Discussion

In summary, we successfully demonstrate an ATS-FET that significantly overcomes the fundamental thermionic limitation of the SS. This ATS-FET achieves extremely abrupt steepness in the turn on characteristics with a typical SS_{average} of 4.5 mV decade $^{-1}$ for more than five decades of I_D at room temperature, and exhibits a significant off-state leakage current reduction to lower the power dissipation. According to the analysis of the I – V dynamics in the ATS-FET both in experiment and simulation, the NDR effect from the TS transition can contribute to inducing an internal V_D , amplification across the MoS₂ channel, enabling the ATS-FET to break the “Boltzmann tyranny”.

As a benefit of the active materials in atomic scale (MoS₂ and Ag filament), the proposed ATS-FET permits the critical scaling of the supply voltage and exhibits superior electrical performances, as well as greatly suppressed off-state current (Supplementary Fig. 11). In addition, the V_D can be readily scaled by reducing the HfO₂ thickness of TS, but the abrupt SS behavior can be

maintained independent of the variable HfO₂ thickness (Supplementary Fig. 12). The geometry design with seamless integration of FET and TS is promising for the potential monolithic integration of the ATS-FET in wafer scale. In this work, the sharp on/off switching properties with ultralow SS in the ATS-FET is originated from the threshold-switching behavior with an internal voltage amplifier, which is universal and applicable to other emerging 2D semiconducting materials related FETs and even different types of transistor devices. To meet the practical applications of logic circuits (also illustrated in the ITRS), the ATS-FETs are available with additional optimization from technical aspects, e.g., further decreasing off current, SS and hysteresis, and improving on/off ratio and reliability. Based on the simulated analysis (Supplementary Fig. 13 and Note 2), the ATS-FET with hysteresis-free behavior is possible to be achieved. Alternatively, in the case of the steep-slope FETs with hysteresis, they could be potentially used as memory devices⁵² or some specific logic circuits, e.g., Schmitt trigger⁵³. Looking forward, the achievement of an ultralow-power steep-slope ATS-FET would coordinate with the scientific research of short-channel devices to efficiently reduce power dissipation, which is highly desirable for next-generation energy-efficient integrated circuits and ultralow-power electronics.

Methods

Device fabrication. The MoS₂ nanoflakes were initially synthesized on highly p-doped rigid silicon (Si) substrates with a thermally grown 275 nm-thick SiO₂ layer through CVD. Copolymer and polymethyl methacrylate was spin-coated at a speed of 4000 r.p.m. and then baked on a hot plate at 150 °C. Subsequently, the source–drain electrodes of the MoS₂ transistor and the BEs of the TS were simultaneously defined with a standard EBL process, thermal evaporation of Cr/Au (10/40 nm), and lift-off process. A dielectric HfO₂ layer of 5–20 nm was fabricated via ALD (PICOSUN/SUNALE R-200) approach. A pre-deposited seed layer of 1 nm of Al via thermal evaporation could help to obtain a high-quality dielectric film. The top gate electrodes of the MoS₂ transistor were defined by a second EBL process and metallization of Cr/Au (10/40 nm). The top electrodes of the TS were defined by a third EBL process and metallization of Ag/Au (3/40 nm).

For the TS device with highly ordered Ag nanodots, an ultrathin AAO template was transferred onto the prepared layers after the step of ALD, and then patterned an Ag thin film (4 nm), and followed by a process of rapid thermal annealing (500 °C for 30 s) after the removal of AAO template. The bottom and top electrodes were fabricated following the above-described process. The as-fabricated TS device can be connected to a baseline FET (MoS₂, monolayer or multilayer) to construct the ATS-FET.

Materials characterization and electrical measurements. The Raman spectrum was measured by a HORIBA/LabRAM HR Evolution spectrograph with a 532 nm excitation laser. The cross-sectional HAADF-STEM image and EDS line profiles of the TS were obtained by STEM (FEI Tecnai F20). The SEM image was captured by a FEI Nova 450. And the EBL was performed by the FEI Nova 450 with a Raith pattern generator. The electrical measurements of the transistors were performed on a probe station equipped with a semiconductor parameter analyzer (Agilent B1500A) in an ambient atmosphere at room temperature.

Data availability

All data supporting this study and its findings are available within the article and its Supplementary Information or from the corresponding author upon reasonable request.

Code availability

The codes that support the findings of this study are available from the corresponding author upon reasonable request.

Received: 3 May 2019; Accepted: 11 November 2020;

Published online: 04 December 2020

References

1. International Technology Roadmap for Semiconductors 2.0 <http://www.itrs2.net/itrs-reports.html> (2015).
2. Sakurai, T. Perspectives of low-power VLSI's. *IEICE T. Electron.* **E87C**, 429–436 (2004).

3. Chang, L. et al. Practical strategies for power-efficient computing technologies. *Proc. IEEE* **98**, 215–236 (2010).
4. Lundstrom, M. Moore's law forever? *Science* **299**, 210–211 (2003).
5. Desai, S. B. et al. MoS₂ transistors with 1-nanometer gate lengths. *Science* **354**, 99–102 (2016).
6. Tomioka, K. Flat transistor defies the limit. *Nature* **526**, 51 (2015).
7. Ionescu, A. M. & Riel, H. Tunnel field-effect transistors as energy-efficient electronic switches. *Nature* **479**, 329–337 (2011).
8. Sarkar, D. et al. A subthermionic tunnel field-effect transistor with an atomically thin channel. *Nature* **526**, 91–95 (2015).
9. Ko, E., Shin, J. & Shin, C. Steep switching devices for low power applications: negative differential capacitance/resistance field effect transistors. *Nano Converg.* **5**, 2 (2018).
10. Chhowalla, M., Jena, D. & Zhang, H. Two-dimensional semiconductors for transistors. *Nat. Rev. Mater.* **1**, 16052 (2016).
11. Fiori, G. et al. Electronics based on two-dimensional materials. *Nat. Nanotechnol.* **9**, 768–779 (2014).
12. Iannaccone, G., Bonaccorso, F., Colombo, L. & Fiori, G. Quantum engineering of transistors based on 2D materials heterostructures. *Nat. Nanotechnol.* **13**, 183–191 (2018).
13. Radisavljevic, B. et al. Single-layer MoS₂ transistors. *Nat. Nanotechnol.* **6**, 147–150 (2011).
14. Gopalakrishnan, K., Griffin, P.B. & Plummer, J.D. I-MOS: a novel semiconductor device with a subthreshold slope lower than kT/q . In *Proc. Digest. International Electron Devices Meeting (IEDM)*, 289–292 (IEEE, San Francisco, CA, USA, 2002).
15. Kim, J. H. et al. Three-terminal nanoelectromechanical field effect transistor with abrupt subthreshold slope. *Nano Lett.* **14**, 1687–1691 (2014).
16. Qiu, C. et al. Dirac-source field-effect transistors as energy-efficient, high-performance electronic switches. *Science* **361**, 387–392 (2018).
17. Salahuddin, S. & Datta, S. Use of negative capacitance to provide voltage amplification for low power nanoscale devices. *Nano Lett.* **8**, 405–410 (2008).
18. McGuire, F. A. et al. Sustained sub-60 mV/decade switching via the negative capacitance effect in MoS₂ transistors. *Nano Lett.* **17**, 4801–4806 (2017).
19. Si, M. et al. Steep-slope hysteresis-free negative capacitance MoS₂ transistors. *Nat. Nanotechnol.* **13**, 24–28 (2018).
20. Wang, X. et al. Van der Waals negative capacitance transistors. *Nat. Commun.* **10**, 3037 (2019).
21. Shukla, N. et al. A steep-slope transistor based on abrupt electronic phase transition. *Nat. Commun.* **6**, 7812 (2015).
22. Song, J. et al. Monolithic integration of AgTe/TiO₂ based threshold switching device with TiN liner for steep slope field-effect transistors. In *Proc. 2016 IEEE Int. Electron Devices Meet. (IEDM)*, 25.3.1–25.3.4 (IEEE, San Francisco, CA, 2017).
23. Grisafe, B. et al. A steep slope phase-FET based on 2D MoS₂ and the electronic phase transition in VO₂. In *2017 International Symposium on VLSI Technology, Systems and Application (VLSI-TSA)*, 1–2 (IEEE, Hsinchu, 2017).
24. Wang, Z. et al. Threshold switching of Ag or Cu in dielectrics: materials, mechanism, and applications. *Adv. Funct. Mater.* **28**, 1704862 (2018).
25. Midya, R. et al. Anatomy of Ag/Hafnia-based selectors with 1010 nonlinearity. *Adv. Mater.* **29**, 1604457 (2017).
26. Hua, Q. et al. A threshold switching selector based on highly ordered Ag nanodots for X-point memory applications. *Adv. Sci.* **6**, 1900024 (2019).
27. Hua, Q. et al. Low-voltage oscillatory neurons for memristor-based neuromorphic systems. *Glob. Chall.* **3**, 1900015 (2019).
28. Lim, S. et al. Excellent threshold switching device ($I_{off} \sim 1$ pA) with atom-scale metal filament for steep slope (<5 mV/dec), ultra low voltage ($V_{dd} = 0.25$ V) FET applications. In *2016 IEEE Int. Electron Devices Meet. (IEDM)*, 34.7.1–37.7.4 (IEEE, San Francisco, CA, 2017).
29. Perera, M. M. et al. Improved carrier mobility in few-layer MoS₂ field-effect transistors with ionic-liquid gating. *ACS Nano* **7**, 4449–4458 (2013).
30. Yang, Y. et al. Electrochemical dynamics of nanoscale metallic inclusions in dielectrics. *Nat. Commun.* **5**, 4232 (2014).
31. Walczyk, C. et al. Impact of temperature on the resistive switching behavior of embedded HfO₂-based RRAM devices. *IEEE Trans. Electron Devices* **58**, 3124–3131 (2011).
32. Long, B. et al. Switching dynamics and charge transport studies of resistive random access memory devices. *Appl. Phys. Lett.* **101**, 113503 (2012).
33. Chiyui, A. et al. Temperature-dependent studies of the electrical properties and the conduction mechanism of HfOx-based RRAM. In *2014 International Symposium on VLSI Technology, Systems and Application (VLSI-TSA)*, 1–2 (IEEE, Hsinchu, 2014).
34. Jiang, C. et al. A closed form analytical model of back-gated 2-D semiconductor negative capacitance field effect transistors. *IEEE J. Electron Devices* **6**, 189–194 (2018).
35. Wang, W. et al. Volatile resistive switching memory based on Ag ion drift/diffusion—PART II: COmpact modeling. *IEEE Trans. Electron Devices* **66**, 3802–3808 (2019).
36. Wang, W. et al. Modeling of switching speed and retention time in volatile resistive switching memory by ionic drift and diffusion. In *2019 IEEE Int. Electron Devices Meet. (IEDM)*, 32.3.1–32.3.4 (IEEE, San Francisco, CA, USA, 2020).
37. Late, D. J. et al. Hysteresis in single-layer MoS₂ field effect transistors. *ACS Nano* **6**, 5635 (2012).
38. Roh, J. et al. Negligible hysteresis of molybdenum disulfide field-effect transistors through thermal annealing. *J. Inf. Disp.* **17**, 103 (2016).
39. Tomioka, K., Yoshimura, M. & Fukui, T. Steep-slope tunnel field-effect transistors using III–V nanowire/Si heterojunction. In *2012 Symp. VLSI Technology (VLSIT)*, 47–48 (IEEE, Honolulu, HI, 2012).
40. Robbins, M. C. & Koester, S. J. Crystal-oriented black phosphorus TFETs with strong band-to-band-tunneling anisotropy and subthreshold slope nearing the thermionic limit. In *2017 IEEE Int. Electron Devices Meet. (IEDM)*, 15.7.1–15.7.4 (IEEE, San Francisco, CA, 2018).
41. Liu, X. et al. MoS₂ negative-capacitance field-effect transistors with subthreshold swing below the physics limit. *Adv. Mater.* **30**, 1800932 (2018).
42. Yu, Z. et al. Negative capacitance 2D MoS₂ transistors with sub-60 mV/dec subthreshold swing over 6 orders, 250 μ A/ μ m current density, and nearly-hysteresis-free. In *2017 IEEE Int. Electron Devices Meet. (IEDM)*, 23.6.1–23.6.4 (IEEE, San Francisco, CA, 2018).
43. Si, M. et al. Steep-slope WSe₂ negative capacitance field-effect transistor. *Nano Lett.* **18**, 3682–3687 (2018).
44. McGuire, F. A. et al. Sub-60 mV/decade switching in 2D negative capacitance field-effect transistors with integrated ferroelectric polymer. *Appl. Phys. Lett.* **109**, 093101 (2016).
45. Wang, X. et al. Two-dimensional negative capacitance transistor with polyvinylidene fluoride-based ferroelectric polymer gating. *npj 2D Mater. Appl.* **1**, 38 (2017).
46. Cheng, C. H. & Chin, A. Low-voltage steep turn-on pMOSFET using ferroelectric high-k gate dielectric. *IEEE Electron Device Lett.* **35**, 274–276 (2014).
47. Park, J. et al. NbO₂ based threshold switch device with high operating temperature (>85 °C) for steep-slope MOSFET (~ 2 mV/dec) with ultra-low voltage operation and improved delay time. In *2017 IEEE Int. Electron Devices Meet. (IEDM)*, 23.7.1–23.7.4 (IEEE, San Francisco, CA, 2018).
48. Yoo, J., Lee, D., Park, J., Song, J. & Hwang, H. Steep slope field-effect transistors with B-Te-based ovonic threshold switch device. *IEEE J. Electron Devices* **6**, 821–824 (2018).
49. Shukla, N. et al. Ag/HfO₂ based threshold switch with extreme non-linearity for unipolar cross-point memory and steep-slope phase-FET. In *2016 IEEE Int. Electron Devices Meet. (IEDM)*, 34.6.1–34.6.4 (IEEE, San Francisco, CA, 2017).
50. Huang, Q. et al. Resistive-gate field-effect transistor: a novel steep-slope device based on a metal-insulator-metal-oxide gate stack. *IEEE Electron Device Lett.* **35**, 877–879 (2014).
51. Wang, X.-F. et al. Two-mode MoS₂ filament transistor with extremely low subthreshold swing and record high on/off ratio. *ACS Nano* **13**, 2205–2212 (2019).
52. Choi, M. S. et al. Controlled charge trapping by molybdenum disulfide and graphene in ultrathin heterostructured memory devices. *Nat. Commun.* **4**, 1624 (2013).
53. Bubel, S. et al. Schmitt trigger using a self-healing ionic liquid gated transistor. *Adv. Mater.* **27**, 3331 (2015).

Acknowledgements

This work is supported in part by the National Science Foundation of China (61904012, 61904164, 61851404, 61874169, and 52073031), the Natural Science Foundation of Beijing Municipality (4204114), the National Key Research and Development Program of China (2016YFA0201800 and 2016YFA0202703), the Fundamental Research Funds for the Central Universities (E0EG6801X2), and the Beijing Nova Program (Z191100001119047).

Author contributions

Q.H. conceived the idea. Q.H. and G.G. designed the experiments. G.G., Q.H., and J.Y. conducted device fabrication. Q.H. performed all data measurements. C.J. did device simulations. J.Y., R.L., T.Z., J.S., and W.C. assisted with the experiments. Q.H., G.G., C.J., B.G., and Q.S. did data analysis. Q.H. and Q.S. drafted the manuscript. H.Q., H.W., W.H., Q.S., and Z.L.W. supervised this work. All the authors discussed the results and commented on the manuscript.

Competing interests

The authors declare no competing interests.

Additional information

Supplementary information is available for this paper at <https://doi.org/10.1038/s41467-020-20051-0>.

Correspondence and requests for materials should be addressed to B.G., Q.S., Z.L.W. or H.W.

Peer review information *Nature Communications* thanks the anonymous reviewers for their contribution to the peer review of this work.

Reprints and permission information is available at <http://www.nature.com/reprints>

Publisher's note Springer Nature remains neutral with regard to jurisdictional claims in published maps and institutional affiliations.



Open Access This article is licensed under a Creative Commons Attribution 4.0 International License, which permits use, sharing, adaptation, distribution and reproduction in any medium or format, as long as you give appropriate credit to the original author(s) and the source, provide a link to the Creative Commons license, and indicate if changes were made. The images or other third party material in this article are included in the article's Creative Commons license, unless indicated otherwise in a credit line to the material. If material is not included in the article's Creative Commons license and your intended use is not permitted by statutory regulation or exceeds the permitted use, you will need to obtain permission directly from the copyright holder. To view a copy of this license, visit <http://creativecommons.org/licenses/by/4.0/>.

© The Author(s) 2020